Research Article

Access to Sb^{III}-containing polyoxotungstates with structure-dependent catalytic enhancement toward Knoevenagel condensation

Han-Feng Meng[1], Yue Ding[1], Qian Chen[1], Yang Wu[1], Xiang-Yu Ren[1,2,], Chao-Qin Chen[1], Jing Du[3], and Peng Yang[1,2,*]*

[1] College of Chemistry and Chemical Engineering, Hunan University, Changsha 410082, China

[2] Greater Bay Area Institute for Innovation, Hunan University, Guangzhou 511300, China

[3] Testing and Analysis Center, Hebei Normal University, Shijiazhuang 050024, China

Received: 4 August 2026; **Revised:** 2 September 2026; **Accepted:** 11 September 2026

*Address correspondence to Xiang-Yu Ren, 1748446842@qq.com; Peng Yang, pengyang216@hnu.edu.cn

Cite This: ***Polyoxometalates*****, 2027, *6*, 9140161**

https://doi.org/10.26599/POM.2026.9140161

Abstract

Owing to the unique lone-pair effect and pronounced hydrolytic tendency, the controllable synthesis of Sb^{III}-containing polyoxometalates (POMs) remains a significant challenge. Rather than being confined as internal heterogroup, the employment of Sb^{III} as an accessible metal center that cooperates with the POM framework represents an emerging research frontier. In this work, a series of Sb^{III}-containing polyoxotungstates were successfully prepared, displaying a systematic structural evolution from dimeric to trimeric assemblies with tunable Sb content. Benefiting from the introduction of strongly Lewis acidic Sb^{III} centers, the obtained POMs, serving as Lewis acid-base catalysts, exhibited significantly enhanced catalytic activity, broad substrate scope, and excellent recyclability in the Knoevenagel condensation reaction. Based on the structure-activity relationship analysis, it is

believed that modulation of the coordination environment around the Sb^{III} centers might serve as a promising strategy for the optimization of catalytic performance.

Keywords: polyoxometalates, polyoxotungstates, antimony, Lewis acid-base catalysis, Knoevenagel condensation

1 Introduction

As molecular models of metal oxides, polyoxometalates (POMs) represent a unique class of metal–oxo clusters characterized by exceptional structural and compositional diversity [1-3]. Thanks to the redox-active metal centers, rigid and stable frameworks, and electron-storage capability, POMs exhibit outstanding performance in various strategic fields such as catalysis, energy, biomedicine, and materials science [4-10]. Upon this, the oxygen-rich surface and intrinsic nucleophilic nature of POMs enable further assembly with exogenous electrophilic reagents [11-14]. The integration of luminescent rare-earth metals, magnetic transition metals, or bioactive organometallic fragments with POMs simultaneously broadens their structural repertoire and functional horizon. Lately, the scope of synergistic electrophiles has been further expanded beyond *d*- and *f*-block elements, with the studies on *p*-block metal-functionalized POMs gradually emerging as a research frontier [15,16].

It has been well established that Sb^{III} ions feature unique redox activity and Lewis acidity, affording applications in pharmaceutical development, organic catalysis, and advanced optoelectronic materials [17-19]. By virtue of the distinctive lone-pair effect, the oxyanions of Sb^{III} (e.g., SbO_3^{3-}) have been widely adopted as heterogroups in the templated synthesis of lacunary POMs [15]. Yet, the incorporation of Sb^{III} atoms is not only limited in quantity but also confined to internal sites, thereby restricting their accessibility toward other reactants. Moreover, it is noteworthy that the number of Sb^{III}-substituted POMs (beyond those serving as heterogroups) remains very limited compared with their 3*d*/4*f*-metal-modified counterparts [20-33]. This is primarily attributed to the strong hydrolytic tendency of Sb^{III} ions, which readily undergo self-polymerization to form insoluble oxide precipitates during the reaction with POMs, thereby posing a significant challenge to the controllable synthesis of such compounds. Besides, the full catalytic potential of Sb^{III}-containing POMs remains to be unlocked [34]. The electrostatic repulsion arising from the lone pair distorts the otherwise highly symmetric coordination environment,

resulting in reduced steric hindrance and exposed accessible sites that favor various metal-based catalytic systems. However, such advantages have not yet been fully exploited.

To address the above issues, herein the di-vacant polyoxotungstate of $[As^{III}_2W_{19}O_{67}(H_2O)]^{14-}$ (As_2W_{19}) was employed to react with potassium antimony tartrate ($K_2Sb_2(tart)_2$), yielding a family of Sb^{III}-containing POMs with varying Sb/W stoichiometries. During the assembly process, the structurally adaptable As_2W_{19} precursor could be reshaped into various building blocks, enriching the binding modes with Sb^{III} ions. Meanwhile, the protective effect of tartrate ligand could suppress the rapid hydrolysis of Sb^{III}, thereby increasing the effective concentration in the reaction. By modulating the reaction variables, the as-prepared POMs exhibit an ordered structural evolution from dimer to trimer, accompanied by a progressive increase in the number of Sb^{III} centers. In consideration of the strong Lewis acidity of Sb^{III}, the catalytic performance of these POMs in Knoevenagel condensation reaction have been systematically investigated. Based on a combination of structural and catalytic studies, the structural determinants that govern catalytic performance have been preliminarily identified. The established structure-activity relationship provides a valuable blueprint for the optimization of Sb^{III}-based POM catalysts.

2 Experimental

General Procedures. The precursor of $K_{14}[As_2W_{19}O_{67}(H_2O)]$ was synthesized according to a published procedure [35]. Other chemicals and reagents were purchased from commercial suppliers and used without further purification. Details about the physical characterizations including single-crystal X-ray diffraction (XRD), Fourier transform infrared (FT-IR) spectroscopy, elemental analysis, X-ray photoelectron spectroscopy (XPS), NMR spectroscopy, energy dispersive X-ray spectroscopy (EDX), powder XRD, and thermogravimetric analysis (TGA) can be found in the supporting information.

Synthesis of $K_{12}Na_4(NH_4)_4[\{Sb(tart)_2\}_2\{(WO_2)_2(AsW_9O_{33})\}_2]\cdot 20H_2O$ (Sb-1). As_2W_{19} (1.0564 g, 0.2 mmol) was dissolved in NaCl solution (10 mL, 0.5 M), and $K_2Sb_2(tart)_2\cdot 3H_2O$ (0.1336 g, 0.2 mmol) was dissolved in HCl solution (0.5 mL, 6 M), respectively. The latter was added to the former solution dropwise and then stirred for 15 min. Then the pH was adjusted to 4.8 using 1 M HCl solution. After stirring for another 10 min, the solution was kept at 80 ℃ for 2 h and cooled to room temperature. NH_4Cl (3-5 drops, 1 M) was added to

the solution after filtration. Slow evaporation of the filtrate in an open vial resulted in colorless rod-shaped crystals after about one week, which were then collected by filtration, washed with cold water and air dried. Yield: 0.108 g (15% based on $K_2Sb_2(tart)_2 \cdot 3H_2O$). Elemental analysis (%): Calcd: K 6.52, Na 1.28, Sb 3.38, As 2.08, W 56.18, C 2.67, N 0.78; Found: K 6.21, Na 1.08, Sb 3.28, As 2.05, W 55.97, C 2.92, N 0.91. IR (2% KBr pellet, ν/cm^{-1}): 3381 (m), 1622 (s), 1361 (m), 1116 (w), 1070 (w), 959 (m), 862 (m), 786 (m), 484 (m).

Synthesis of $K_{10}[(SbOH)_2\{As_2W_{19}O_{67}(H_2O)\}] \cdot 23H_2O$ (Sb-2).

As_2W_{19} (1.0564 g, 0.2 mmol) was dissolved in 10 mL water, and $K_2Sb_2(tart)_2 \cdot 3H_2O$ (0.1336 g, 0.2 mmol) was dissolved in HCl solution (0.5 mL, 6 M), respectively. The latter was added to the former solution dropwise and then stirred for 15 min. Then the pH was adjusted to 4.0 using 1 M HCl solution. After stirring for another 10 min, the solution was kept at 80 ℃ for 2 h and cooled to room temperature. Slow evaporation of the filtrate in an open vial resulted in yellow rod-shaped crystals after about one week, which were then collected by filtration, washed with cold water and air dried. Yield: 0.128 g (11% based on $K_2Sb_2(tart)_2 \cdot 3H_2O$). Elemental analysis (%): Calcd: K 6.72, Sb 4.19, As 2.58, W 60.06; Found: K 6.98, Sb 4.01, As 2.32, W 59.35. IR (2% KBr pellet, ν/cm^{-1}): 3390 (m), 953 (m), 871 (m), 714 (s), 495 (m).

Synthesis of $K_{10}Na_2[(SbCl)_3(AsW_9O_{33})_2] \cdot 28H_2O$ (Sb-3).

As_2W_{19} (1.0564 g, 0.2 mmol) was dissolved in NaCl solution (10 mL, 0.5 M), and $K_2Sb_2(tart)_2 \cdot 3H_2O$ (0.1336 g, 0.2 mmol) was dissolved in HCl solution (0.5 mL, 6 M), respectively. The latter was added to the former solution dropwise and then stirred for 15 min. Then the pH was adjusted to 5.0 using 1 M HCl solution. After stirring for another 10 min, the solution was kept at 80 ℃ for 2 h and cooled to room temperature. Slow evaporation of the filtrate in an open vial resulted in yellow rhombic crystals after about one week, which were then collected by filtration, washed with cold water and air dried. Yield: 0.071 g (9% based on $K_2Sb_2(tart)_2 \cdot 3H_2O$). Elemental analysis (%): Calcd: K 6.60, Na 0.77, Cl 1.79, Sb 6.16, As 2.53, W 55.82; Found: K 6.37, Na 0.92, Cl 1.14, Sb 6.21, As 2.45, W 56.03. IR (2% KBr pellet, ν/cm^{-1}): 3416 (m), 950 (m), 848 (m), 726 (s), 467 (m).

Synthesis of $K_{20}Na_3[\{Sb(tart)\}_4(SbOH)(WO_2)_4(AsW_9O_{33})_3] \cdot Sb_2(tart)_2 \cdot 22H_2O$ (Sb-4).

Sb-4 was synthesized by the same procedure as **Sb-3**, except adjusting the reaction pH to 4.5. Slow evaporation of the filtrate in an open vial resulted in colorless rod-shaped crystals after

about one week, which were then collected by filtration, washed with cold water and air dried. Yield: 0.073 g (12% based on $K_2Sb_2(tart)_2 \cdot 3H_2O$). Elemental analysis (%): Calcd: K 7.36, Na 0.65, Sb 8.02, As 2.11, W 53.62, C 2.71; Found: K 7.45, Na 0.52, Sb 7.89, As 2.18, W 53.24, C 2.59. IR (2% KBr pellet, ν/cm^{-1}): 3401 (m), 1628 (s), 1357 (m), 1067 (w), 965 (m), 868 (m), 791 (m), 711 (m), 481 (m).

3 Results and Discussion

Synthesis and Structure. All of the compounds were prepared by a facile one-pot synthetic approach. It has been experimentally proved that, despite both As_2W_{19} and $K_2Sb_2(tart)_2$ underwent dissociation to varying degrees, neither component could be replaced. The use of similar precursors, such as $[B\text{-}a\text{-}As^{III}W_9O_{33}]^{9-}$ (AsW_9) or Sb_2O_3, failed to yield the target compounds, presumably owing to the dynamic equilibrium established between the two specific reactants. Furthermore, pH was identified as a decisive parameter in the reaction, determining both the speciation of the As_2W_{19}-derived building blocks and the hydrolysis kinetic of Sb^{III}. This dual influence enables effective control over the assembly pathway and resulting structures. In addition, the type of counter cations and reaction solutions were found to affect both the crystallization outcome and isolated yield as well.

Single-crystal XRD revealed that $[\{Sb(tart)_2\}_2\{(WO_2)_2(AsW_9O_{33})\}_2]^{20-}$ (**Sb-1**) adopts a typical dimeric archetype (Fig. 1a). A pair of $\{WO_6\}$ units are attached on the vacant sites of the AsW_9 fragment, resulting in a mono-vacant species of $\{(WO_2)_2(AsW_9O_{33})\}$ (AsW_{11}). Upon this, two $\{Sb(tart)_2\}$ arms are each coordinated to the aforementioned $\{WO_6\}$ units via the carboxylate groups of the tartrate ligands, thereby linking the two AsW_{11} fragments into a dimeric structure. Upon adjusting the reaction pH to 4.0 and 5.0, respectively, the dimeric $[(SbOH)_2\{As_2W_{19}O_{67}(H_2O)\}]^{10-}$ (**Sb-2**) and $[(SbCl)_3(AsW_9O_{33})_2]^{12-}$ (**Sb-3**) were isolated. For **Sb-2**, the intact framework of As_2W_{19} is fully retained, with a pair of Sb^{III} atoms occupying the two lacunary sites, resulting in an overall structure with a C_{2v} point group symmetry (Fig. 1b). A structure similar to **Sb-2** was recently reported by Han et al., which crystallized in a different cationic and solvent system [36]. In contrast to **Sb-2**, the structure of **Sb-3** involves the replacement of the W center located at the belt position of As_2W_{19} by a third Sb^{III} atom. Hence the three Sb^{III} centers are uniformly arranged around the equatorial plane, and the two AsW_9 fragments are rotated by 60° with respect to each other, affording a sandwich-type

assembly with idealized C_{3v} symmetry (Fig. 1c). Besides, a trimeric assembly of $[\{Sb(tart)\}_4(SbOH)(WO_2)_4(AsW_9O_{33})_3]^{21-}$ (**Sb-4**) was obtained at pH 4.5, in which the three AsW_9 fragments are arranged in a triangular fashion (Fig. 1d). Building upon this, the released $\{WO_6\}$ units occupy the partial vacant sites of AsW_9 to afford one AsW_{11}- and two AsW_{10}-type building blocks (Fig. S1). Their remaining vacancies are filled by five Sb^{III} ions. Subsequently, the three components are bridged together by four tartrate ligands. Each of them adopts the binding mode analogous to that in **Sb-1**, with the two ends coordinating to one W and one Sb center, respectively. In addition, a discrete $[Sb_2(tart)_2]^{2-}$ anion was found to co-crystallize with such trimeric assembly (Fig. S2). Collectively, these findings demonstrate that the type and number of POM fragments can be effectively modulated by tuning the reaction conditions. Notably, even for the structure of **Sb-1~3** that all adopt a dimeric topology, the number and coordination environment of Sb^{III} ions remain further adjustable. Moreover, the tartrate ligand could serve as linker and selectively participate in the construction of metal-oxo frameworks.

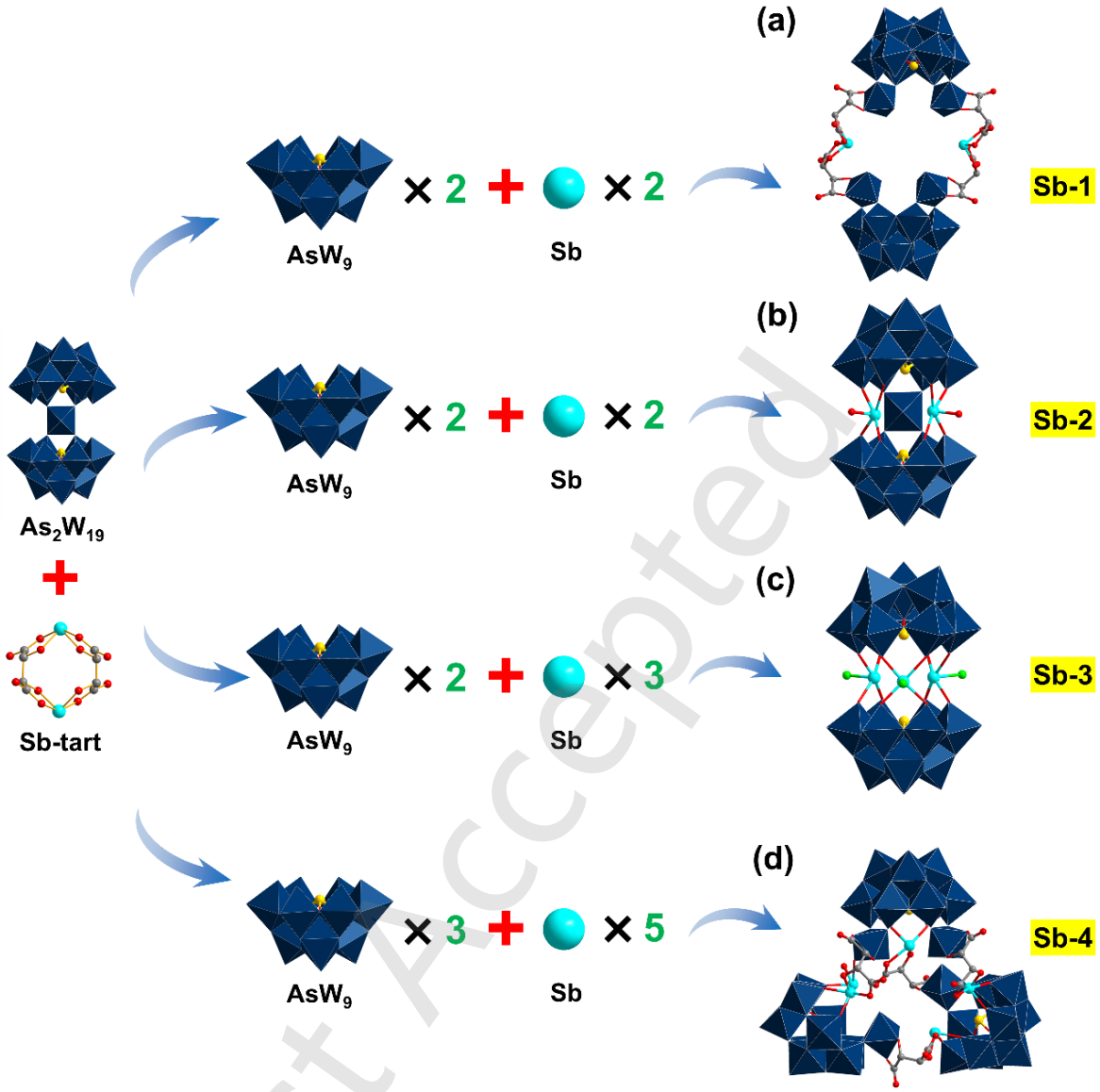

Figure 1 Combined polyhedral/ball-and-stick representation of **Sb-1** (a), **Sb-2** (b), **Sb-3** (c), and **Sb-4** (d). Color code: {WO_6}, teal octahedra; Sb, turquoise; As, yellow; Cl, green; O, red; C, grey balls. Hydrogen atoms are omitted for clarity.

A closer inspection showcased that the Sb^{III} centers in the as-made POMs adopt two types of coordination geometries, namely four-coordinate seesaw and five-coordinate square-pyramidal configurations. It has been noted that the lone pairs on all Sb^{III} centers are oriented toward the interior of the POM frameworks, which is consistent with the previous observations in Sb^{III}-containing POMs [24-29]. Specifically, the coordination sphere of the Sb^{III} ions in **Sb-1** is completed by four oxygen atoms from the tartrate ligands (Fig. 2a). For **Sb-2** and **Sb-3**, the equatorial plane of the Sb^{III} ions involved are fixed by four oxo groups, while the axial position is occupied by a hydroxide or chloride ion, respectively (Figs. 2b and

2c). For **Sb-4**, the five Sb^{III} ions share a similar seesaw geometry but differ in their ligand sets. Four of the Sb^{III} atoms are coordinated by two oxygen atoms (tartrate ligand) and two oxo groups (POM framework), whereas the remaining Sb^{III} center is ligated by three oxo groups and one hydroxide ligand (Figs. 2d and S3). The protonation states of the specific oxygen atoms were determined by bond valence sum (BVS) calculations (Table S1). Obviously, rather than being buried as internal heterogroups, herein the Sb^{III} ions are distributed on the surface of POM structures. In addition to the variation in Sb^{III} content, the diverse coordination environments of the Sb^{III} centers offer an ideal platform for the systematic study of their structure-activity relationships in catalysis.

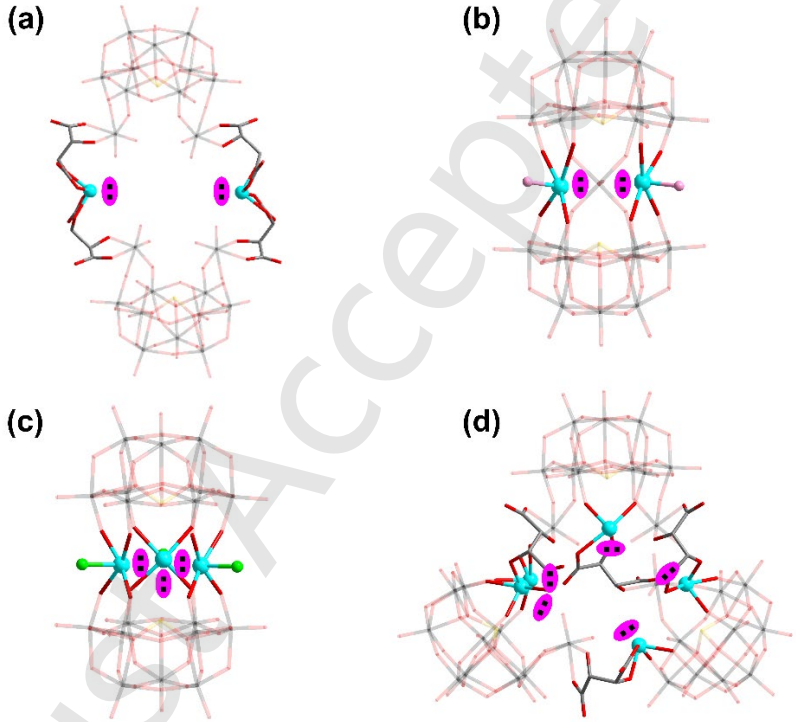

Figure 2 Coordination environment of the Sb^{III} ions in **Sb-1** (a), **Sb-2** (b), **Sb-3** (c), and **Sb-4** (d). Color code: Sb, turquoise; Cl, green; OH, pink balls.

Physical Characterizations. In addition to single-crystal XRD, FT-IR spectroscopy was employed to provide more structural information. As depicted in Fig. 3a, the strong absorption bands at around 1635 and 1365 cm^{-1} are assigned to the asymmetric and symmetric stretching vibrations of the carboxylate groups from the tartrate ligands in **Sb-1** and **Sb-4**, respectively [37-39]. For all the polyanions, the peaks centered at ca. 950 cm^{-1} belong to the Sb–O vibrations, while the peaks located at ca. 860 cm^{-1} correspond to the As−O vibrations [40,41]. The remaining signals below 1000 cm^{-1} can be ascribed to the

stretching modes of terminal W=O and bridging W–O–W moieties [42]. Subsequently, the oxidation states of Sb and W centers were examined by XPS (Fig. S4). Taking **Sb-2** as an example, the binding energies of Sb $3d_{3/2}$ (539.9 eV) and Sb $3d_{5/2}$ (531.5 eV) are consistent with the Sb^{III} oxidation state (Fig. 3b) [34]. Also, the peaks appeared at 37.6 eV (W $4f_{5/2}$) and 35.5 eV (W $4f_{7/2}$) confirm the presence of W^{VI} addenda (Fig. 3c) [42]. Moreover, the elemental mapping images demonstrate that W, Sb, As, Cl are correspondingly distributed in **Sb-3**, further corroborating the identity of the Cl^- ligands on the Sb^{III} centers (Fig. 3d). The thermal stability of the obtained compounds was investigated on crystalline samples by TGA (Fig. 3e). For **Sb-1** and **Sb-4**, the curves exhibit roughly three weight-loss steps, which are attributable to the loss of crystalline water molecules (25-150 °C), decomposition of the organic ligands (340-380 °C), and breakdown of the residual POM framework (420-480 °C), respectively. In contrast, the curves of **Sb-2** and **Sb-3** display simplified two-step weight-loss profiles. For **Sb-3**, the water content determined by TGA exceeds that derived from elemental analysis, which is likely attributable to moisture uptake by the sample. Besides, the powder XRD patterns of the obtained compounds are in good agreement with their simulated data, confirming the phase purity of the bulk materials (Figs. 3f and S5).

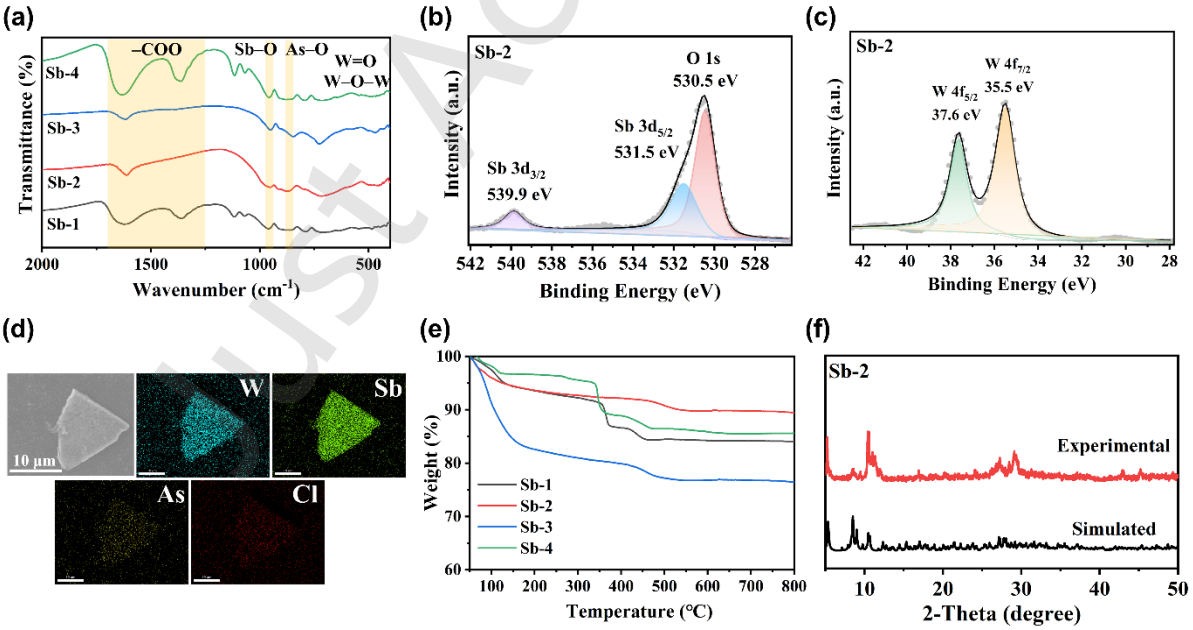

Figure 3 (a) FT-IR spectra of the as-made compounds. (b) XPS spectrum and fits for Sb $3d_{3/2}$ and Sb $3d_{5/2}$ in **Sb-2**. (c) XPS spectrum and fits for W $4f_{5/2}$ and W $4f_{7/2}$ in **Sb-2**. (d) Elemental mapping images of W, Sb, As, Cl in **Sb-3**. (e) Thermograms of the as-made compounds. (f) Powder XRD patterns of **Sb-2**.

Knoevenagel Condensation Catalysis. Knoevenagel condensation represents a widely

employed and powerful strategy for the C=C bond formation via dehydration coupling between carbonyl and methylene substrates [43,44]. Such transformation has found widespread applications in diverse fields, ranging from pharmaceuticals to functional polymeric materials. It has been well documented that the metal centers in POMs can serve as Lewis acids, while the oxygen ligands can function as Lewis bases, and their synergistic cooperation enables efficient catalysis of Knoevenagel condensation reaction [45,46]. In view of the presence of strongly Lewis acidic Sb^{III} ions in the as-made POMs, their catalytic performances were systematically investigated. Firstly, the condensation of benzaldehyde and malononitrile was selected as the model reaction to determine the optimal reaction conditions. To preliminarily evaluate the catalytic activity, the experiments were conducted at room temperature for 1 h using 0.1 mol% **Sb-1~4** as catalysts. As shown in Table 1 (Entry 1-4), the yield of the desired product is 71% (**Sb-1**), 77% (**Sb-2**), 64% (**Sb-3**), and 48% (**Sb-4**), respectively. Therefore, the group of **Sb-2** was selected for further optimization. It was found that extending the reaction time to 2 h significantly increased the yield to 99% (Entry 5-7). Moreover, the optimal solvent and catalyst loading were also confirmed (Entry 8-11). Under the optimized conditions, a control experiment without any catalyst afforded a conversion of 30% (Entry 12). Meanwhile, the use of As_2W_{19}, $K_2Sb_2(tart)_2$, a physical mixture of them as well as $NaSbO_3$ as catalysts resulted in yields of 67%, 35%, 72% and 46%, respectively (Entry 13-16). In sharp contrast, all of the Sb^{III}-containing POMs were found to effectively promote the respective yield to 97% (**Sb-1**), 99% (**Sb-2**), 99% (**Sb-3**), and 88% (**Sb-4**) (Entry 7, 17-19).

Table 1. Condensation of benzaldehyde and malononitrile using different catalysts[a]

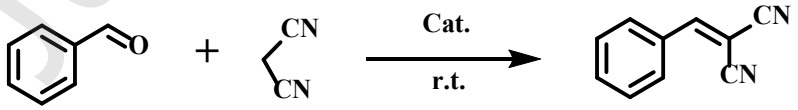

Entry	Catalyst (mol %)	Solvent	Time (h)	Yield (%)[b]
1	**Sb-1** (0.1)	EtOH	1	71
2	**Sb-2** (0.1)	EtOH	1	77
3	**Sb-3** (0.1)	EtOH	1	64
4	**Sb-4** (0.1)	EtOH	1	48
5	**Sb-2** (0.1)	EtOH	0.5	41

6	**Sb-2** (0.1)	EtOH	1.5	90
7	**Sb-2** (0.1)	EtOH	2.0	99
8	**Sb-2** (0.1)	DMF	2.0	84
9	**Sb-2** (0.1)	MeOH	2.0	90
10	**Sb-2** (0.05)	EtOH	2.0	74
11	**Sb-2** (0.2)	EtOH	2.0	99
12	No catalyst	EtOH	2.0	30
13	As_2W_{19} (0.1)	EtOH	2.0	67
14	$K_2Sb_2(tart)_2$ (0.1)	EtOH	2.0	35
15	Mixture (0.1)	EtOH	2.0	72
16	$NaSbO_3$ (0.1)	EtOH	2.0	46
17	**Sb-1** (0.1)	EtOH	2.0	97
18	**Sb-3** (0.1)	EtOH	2.0	99
19	**Sb-4** (0.1)	EtOH	2.0	88

[a] Reaction condition: benzaldehyde (0.1 mmol), malononitrile (0.2 mmol), and EtOH 2 mL. [b] Isolated yields.

Encouraged by the above results, several benzaldehyde derivatives bearing different substituents were employed to further evaluate the universality of the **Sb-2** catalyst. It is obvious that excellent catalytic yields were obtained regardless of whether electron-withdrawing or electron-donating groups are introduced onto the benzaldehyde substrate, or the position of the substituents are varied (Table 2). All the ^{1}H NMR spectra of the products are recorded in the supporting information.

Table 2. Substrate scope of the **Sb-2**-catalyzed Knoevenagel condensation reaction[a,b]

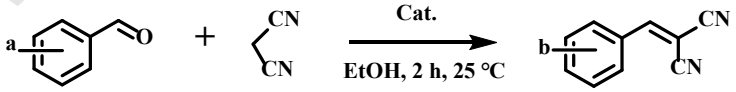

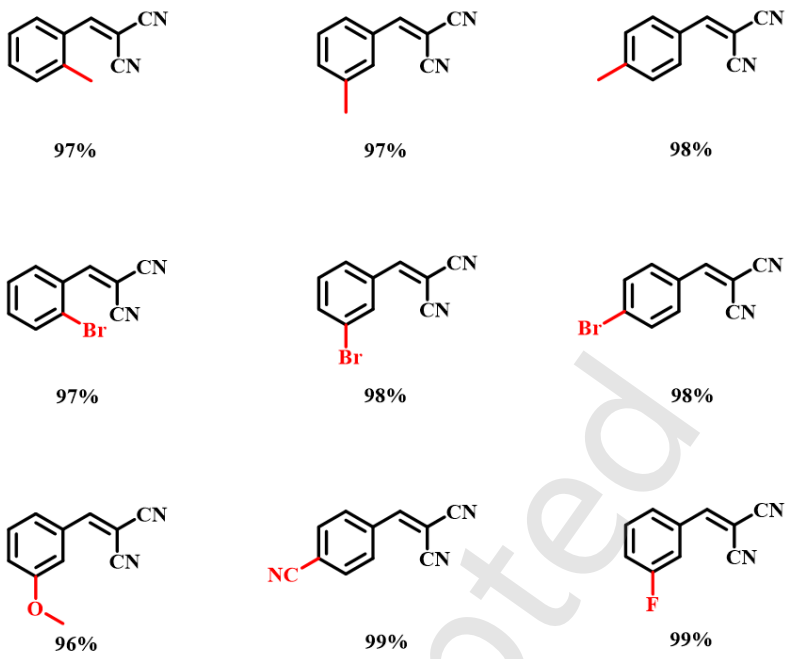

[a] Reaction condition: benzaldehyde (0.1 mmol), malononitrile (0.2 mmol), **Sb-2** (0.1 mol%), and EtOH 2 mL. [b] Isolated yields.

Additionally, the heterogeneous nature of the **Sb-2** catalyst was verified by a hot filtration test. As depicted in Fig. 4a, the yield remains almost unchanged after removal of the catalyst from the reaction at 0.5 h. Moreover, the **Sb-2** catalyst could be reused for at least five consecutive cycles, with the average yield remaining above 95% (Fig. 4b). The gram-scale experiments (10 mmol benzaldehyde and 20 mmol malononitrile) using **Sb-2** as catalyst afforded the yield of 81%. The decrease in catalytic efficiency is most likely attributable to the aggregation of **Sb-2** catalysts under enlarged reaction volumes, which reduces the effective surface area of exposed active sites and consequently leads to a decline in catalytic performance. Comparison of the powder XRD patterns (Figs. 4c) and FT-IR spectra (Figs. 4d and S6) before and after catalysis revealed no apparent differences, confirming the structural integrity of the catalysts. Taken together, these findings establish that the heterogeneous **Sb-2** catalyst possesses outstanding recyclability and structural stability for the Knoevenagel condensation.

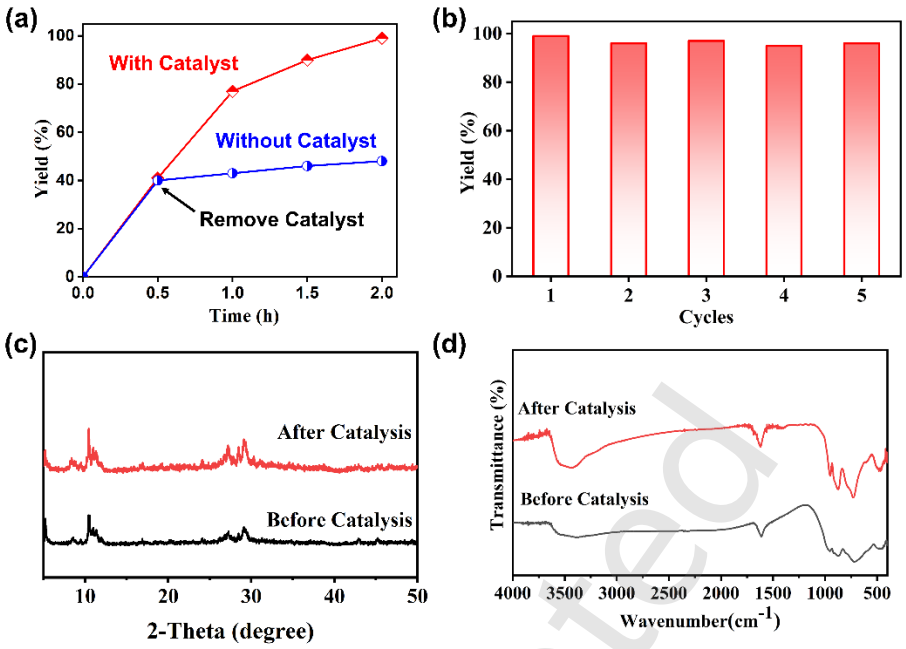

Figure 4 (a) Results of the filtration test conducted on the **Sb-2** heterogeneous catalyst. (b) Catalytic stability of **Sb-2** (error bar ± 1%). (c) Powder XRD patterns of **Sb-2** before and after catalysis. (d) FT-IR spectra of **Sb-2** before and after catalysis.

To further elucidate the structure-activity relationship of the Sb^{III}-containing POM catalysts, the conversion efficiencies were recorded at different time intervals (Fig. 5a). It was found that the dimeric **Sb-2** and **Sb-3** exhibited relatively high catalytic activity (> 40%) within the initial 0.5 h, whereas the monomeric **Sb-1** and trimeric **Sb-4** afforded conversions of only 28% and 16%, respectively. Upon prolonging the reaction time to 2 h, the catalytic efficiency of **Sb-1** gradually increased, whereas no significant improvement was observed for **Sb-4**. A closer look at the composition of the POM catalysts revealed that **Sb-4**, which contains the most W^{VI} atoms, exhibited the lowest activity, suggesting that the W^{VI} addenda might not serve as the primary Lewis-acid centers (Fig. 5b). Likewise, despite having the highest Sb content among all four catalysts, **Sb-4** still failed to deliver the best catalytic performance. To gain insight into this interesting observation, the crystal packing diagrams of the four POMs were examined. As depicted in Fig. S7, all of the polyanions adopt densely packed modes in the solid state, without evidence of significant porosity. Their different catalytic activities are therefore mainly ascribed to the structural variations. Apparently, the highly exposed Sb^{III} centers in **Sb-2** and **Sb-3** would facilitate the interaction with aldehyde substrates as Lewis-acid catalytic sites. By contrast, the surface of the Sb^{III} centers in **Sb-4** are largely covered by tartrate ligands. This might severely restrict the accessibility of substrates

to the Sb^{III} sites and thus suppresses the catalytic efficiency significantly (Fig. 5c) [37]. While the Sb^{III} centers in **Sb-1** are likewise partially shielded by tartrate ligands, the elongated $\{Sb(tart)_2\}$ arms exhibit conformational flexibility. The intrinsic cavity within the structure might facilitate substrate access, thereby rendering its catalytic activity largely unaffected (Fig. 5d). Therefore, it is plausible that the coordination environment around the Sb^{III} centers might play a decisive role in dictating the catalytic performance of the Sb^{III}-POMs. As a consequence, a possible catalytic mechanism is proposed in Fig. 5e. In the beginning, the Lewis acidic Sb^{III} sites contact with the carbonyl oxygen of the aldehyde, while the surface oxygen atoms of the POM framework act as Lewis bases to activate the methylene group of malononitrile via hydrogen bonding, generating a nucleophilic carbon center. Subsequent dehydration affords the benzylidenemalonitrile product and regenerates the POM catalyst for the next cycle.

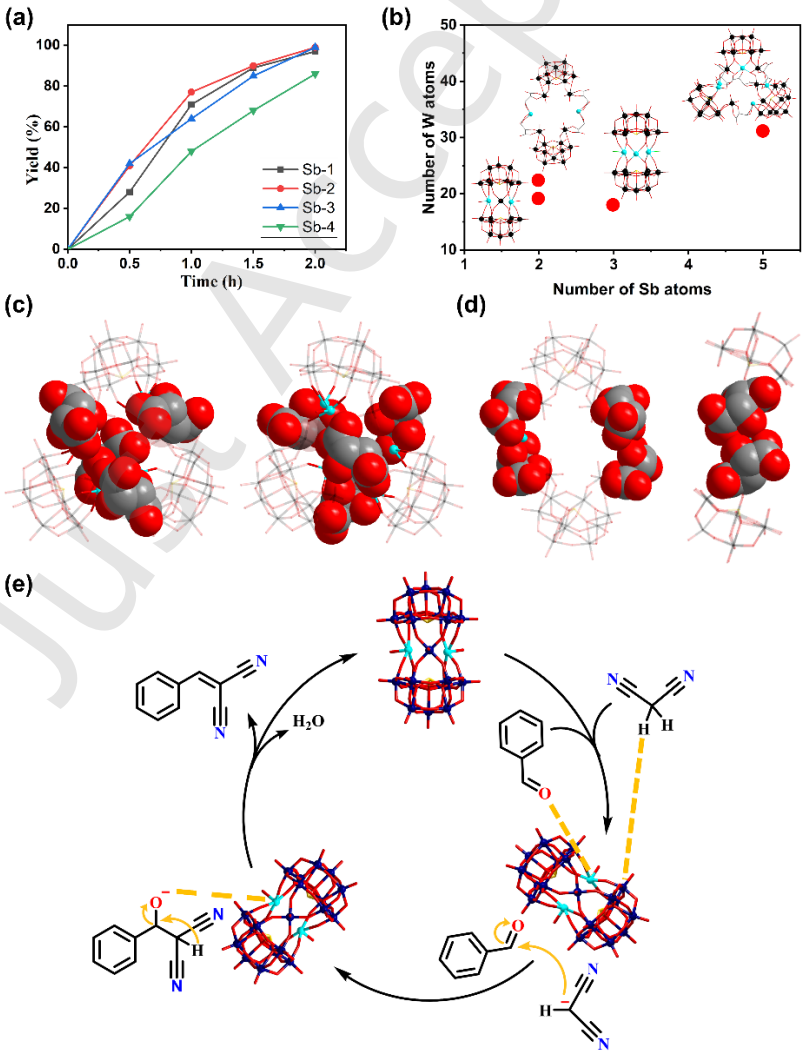

Figure 5 (a) Catalytic conversion efficiencies at different time intervals. (b) Number of metallic centers in different catalysts. (c,d) Coverage of tartrate ligands on the surface of **Sb-4** (c) and **Sb-1** (d). (e) Proposed catalytic mechanism of the Sb^{III}-containing POMs.

4 Conclusions

By the reaction of As_2W_{19} and $K_2Sb_2(tart)_2$, a family of Sb^{III}-containing polyoxotungstates has been successfully isolated and fully characterized. Through precise control of the reaction parameters (e.g., pH), both the aggregation state and Sb^{III} content of these POM assemblies can be systematically tuned. Apart from the structural interests, their catalytic performance as Lewis acid–base catalysts were evaluated in the Knoevenagel condensation reaction. It has been revealed that the incorporation of Sb^{III} ions significantly enhanced the catalytic efficiency of POMs, and the coordination environment around the Sb^{III} centers might play a pivotal role in determining the catalytic efficiency. These findings provide valuable guidance for the synthesis and optimization of main-group-metal-functionalized POM catalysts, as well as for the elucidation of their structure-activity relationships.

Electronic Supplementary Material: Supplementary material (Experimental details, relevant structure figures, tables of BVS calculation data as well as crystal data and structure refinement) is available in the online version of this article at https://doi.org/10.26599/POM.2026.9140161.

Data availability

All data needed to support the conclusions in the paper are presented in the manuscript and/or the Electronic Supplementary Material. Additional data related to this paper may be requested from the corresponding author upon request.

Acknowledgements

This research was financially supported by the National Natural Science Foundation of China (22571076), Guangdong Basic and Applied Basic Research Foundation (2025A1515010370), and the Student Innovation Training (SIT) program (No. 202510532051).

Declaration of competing interest

The authors have no competing interests to declare that are relevant to the content of this article.

Author contribution statement

The manuscript was written through contributions of all authors.

References

1. Pope, M. T. *Heteropoly and Isopoly Oxometalates*; SpringerVerlag: Berlin, 1983.
2. Pope, M. T.; Müller, A. *Polyoxometalate Chemistry: From Topology via Self-Assembly to Applications*; Kluwer Academic Publishers: Dordrecht, Netherlands, 2001.
3. Liu, L. L.; Wang, L.; Xiao, X. Y.; Yang, P.; Zhao, J. W.; Kortz, U. Structural overview and evolution paths of lacunary polyoxometalates. *Coord. Chem. Rev.* **2024**, *506,* 215687.
4. Wang, S. S.; Yang, G. Y. Recent advances in polyoxometalate-catalyzed reactions. *Chem. Rev.* **2015**, *115,* 4893−4962.
5. Li, J.; Zhang, D.; Chi, Y. N.; Hu, C. W. Catalytic application of polyoxovanadates in the selective oxidation of organic molecules. *Polyoxometalates* **2022**, *1,* 9140012.
6. Zhang, Q.; Li, F. Y.; Xu, L. Application of polyoxometalates in third-generation solar cells. *Polyoxometalates* **2023,** *2,* 9140018.
7. Zhang, S. S.; Liu, R. J.; Streb, C.; Zhang, G. J. Design and synthesis of novel polyoxometalate-based binary and ternary nanohybrids for energy conversion and storage. *Polyoxometalates* **2023,** *2,* 9140037.
8. Budych, M. J. W.; Staszak, K.; Bajek, A.; Pniewski, F.; Jastrząb, R.; Staszak, M.; Tylkowski, B.; Wieszczycka, K. The future of polyoxymetalates for biological and chemical applications. *Coord. Chem. Rev.* **2023,** *493,* 215306.
9. Cheng, Y.; Qin, K. J.; Zang, D. J. Polyoxometalates based nanocomposites for bioapplications. *Rare Met.* **2023,** *42,* 3570−3600.
10. Yang, G. P.; Liu, Y. F.; Wei, Y. G. Application of polyoxometalates in biomass conversion. *Coord. Chem. Rev.* **2024,** *521,* 216172.
11. Das, V.; Kaushik, R.; Hussain, F. Heterometallic 3d-4f polyoxometalates: An emerging field with structural diversity to multiple applications. *Coord. Chem. Rev.* **2020,** *143,* 213271.
12. Li, S. R.; Liu, W. D.; Long, L. S.; Zheng, L. S.; Kong, X. J. Recent advances in polyoxometalate-based lanthanide–oxo clusters. *Polyoxometalates* **2023,** *2,* 9140022.
13. Liu, J. C.; Zhao, J. W.; Streb, C.; Song, Y. F. Recent advances on high-nuclear polyoxometalate clusters. *Coord. Chem. Rev.* **2022,** *471,* 214734.
14. Qian, D. Q.; Lin, Y. D.; Xiao, H. P.; Wu, B.; Li, X. X.; Zheng, S. T. Advances in coinage-metal-substituted polyoxometalates: A review. *Polyoxometalates* **2024,** *3,* 9140040.
15. Tang, Z. G.; Tang, M. Y.; Wang, D.; Chen, L. J.; Zhao, J. W. Research progress in trivalent main group V heteroanion-templated polyoxometalates. *Coord. Chem. Rev.* **2026,** *548,* 217156.
16. Tang, Z. G.; Li, J. X.; Wang, D.; Chen, L. J.; Zhao, J. W. Frontier advances in

polyoxometalates templated by main group VI heteroatoms. *Coord. Chem. Rev.* **2026,** *560,* 217880.
17. Fischer, J.; Ricard, L.; Weiss, R. The structure of the heteropolytungstate $(NH_4)_{17}Na[NaW_{21}Sb_9O_{86}]\cdot 14H_2O$. An inorganic cryptate. *J. Am. Chem. Soc.* **1976,** *98,* 3050.
18. Xiao, H. P.; Hao, Y. S.; Li, X. X.; Xu, P.; Huang, M. D.; Zheng, S. T. A water-soluble antimony-rich polyoxometalate with broad-spectrum antitumor activities. *Angew. Chem. Int. Ed.* **2022**, *61,* e202210019.
19. Shi, S. K.; Li, X.; Guo, H. L.; Fan, Y. H.; Li, H. Y.; Dang, D. B.; Bai, Y. Ionothermal synthesis of an antimonomolybdate cluster, $[Sb_8Mo^{VI}_{13}Mo^{V}_5O_{66}]^{5-}$, and its catalytic behavior to the reduction of nitrobenzene. *Inorg. Chem.* **2020**, *59,* 11213−11217.
20. Khenkin, A. M.; Shimon, L. J. W.; Neumann, R. Antimony-substituted Keggin-type polyoxomolybdates: Polar crystals and catalytic oxidative dehydrogenation of alcohols. *Eur. J. Inorg. Chem.* **2001,** 789−794.
21. Hu, X. X.; Xu, J. Q.; Cui, X. B.; Song, J. F.; Wang, T. G. A novel one-dimensional framework material constructed from antimony-substituted polyoxovanadium clusters: $[(C_2N_2H_{10})_2\beta\text{-}\{Sb^{III}_8V^{IV}_{14}O_{42}(H_2O)\}](C_2N_2H_8)\cdot 4H_2O$. *Inorg. Chem. Commun.* **2004,** *7,* 264−267.
22. Zhang, Q. B.; Lu, Y. K.; Liu, Y. B.; Lu, J.; Bi, M. H.; Yu, J. H.; Wang, T. G.; Xu, J. Q.; Liu, J. Synthesis and characterization of the first polyoxometalate possessing bicapped by antimony α-Keggin structure $(C_2N_2H_9)_2[PMo^{V}_5Mo^{VI}_7Sb^{III}_2O_{40}]\cdot 2H_2O$. *Inorg. Chem. Commun.* **2006,** *9,* 544−547.
23. Zhang, C. D.; Liu, S. X.; Ma, F. J.; Tan, R. K.; Zhang, W.; Su, Z. M. Coordination between $[H_2P_2W_{12}O_{48}]^{12-}$ and antimony(III), synthesis and characterization of sandwich complex derived from the new $\{P_2W_{13}O_{51}\}$ fragment. *Dalton Trans*. **2010**, *39*, 8033−8037.
24. Assran, A. S.; Izarova, N. V.; Banerjee, A.; Rabie, U. M.; Abou-El-Wafab, M. H. M.; Kortz, U. The antimony(III)-bridged heteropolyanion sandwich dimers $[Sb^{III}_3(A\text{-}\alpha\text{-}XW_9O_{34})_2]^{11-}$ (X = Si^{IV}, Ge^{IV}) and C-shaped double-sandwich $[Sb^{III}_6O_2(PW_6O_{26})(A\text{-}\alpha\text{-}PW_9O_{34})_2]^{15-}$. *Dalton Trans.* **2012**, *41,* 9914−9921.
25. Barsukova-Stuckart, M.; Piedra-Garza, L. F.; Gautam, B.; Alfaro-Espinoza, G.; Izarova, N. V.; Banerjee, A.; Bassil, B. S.; Ullrich, M. S.; Breunig, H. J.; Silvestru, C.; Kortz, U. Synthesis and biological activity of organoantimony(III)-containing heteropolytungstates. *Inorg. Chem.* **2012,** *51,* 12015−12022.
26. Yang, P.; Bassil, B. S.; Lin, Z. G.; Haider, A.; Alfaro-Espinoza, G.; Ullrich, M. S.; Silvestru, C.; Kortz, U. Organoantimony(III)-containing tungstoarsenates(III): From controlled assembly to biological activity. *Chem. Eur. J.* **2015,** *21,* 15600–15606.
27. Yang, P.; Lin, Z. G.; Alfaro-Espinoza, G.; Ullrich, M. S.; Raţ, C. I.; Silvestru, C.; Kortz, U. 19-Tungstodiarsenate(III) functionalized by organoantimony(III) groups: tuning the structure-bioactivity relationship. *Inorg. Chem.* **2016,** *55,* 251−258.
28. Yang, P.; Lin, Z. G.; Bassil, B. S.; Alfaro-Espinoza, G.; Ullrich, M. S.; Li, M. X.; Silvestru, C.; Kortz, U. Tetra-antimony(III)-bridged 18-tungsto-2-arsenates(V), $[(LSb^{III})_4(A\text{-}\alpha\text{-}As^{V}W_9O_{34})_2]^{10-}$ (L = Ph, OH): Turning bioactivity on and off by ligand substitution. *Inorg. Chem.* **2016,** *55,* 3718−3720.

29. Ma, T.; Yang, P.; Dammann, I.; Lin, Z. G.; Mougharbel, A. S.; Li, M. X.; Adăscăliţei, F.; Mitea, R.; Silvestru, C.; Thorstenson, C.; Ullrich, M. S.; Cseh, K.; Jakupec, M. A.; Keppler, B. K.; Donalisio, M.; Cavalli, R.; Lembo, D.; Kortz, U. Tetra-(p-tolyl)antimony(III)-containing heteropolytungstates, $[\{(p\text{-tolyl})Sb^{III}\}_4(A\text{-}\alpha\text{-}XW_9O_{34})_2]^{n-}$ (X = P, As, or Ge): Synthesis, structure, and study of antibacterial and antitumor activity. *Inorg. Chem.* **2020,** *59,* 2978−2987.
30. Cai, J.; Zheng, X. Y.; Xie, J.; Yan, Z. H.; Kong, X. J.; Ren, Y. P.; Long, L. S.; Zheng, L. S. Anion-dependent assembly of heterometallic 3d−4f clusters based on a lacunary polyoxometalate. *Inorg. Chem.* **2017**, *56,* 8439−8445.
31. Li, S. R.; Wang, H. Y.; Su, H. F.; Chen, H. J.; Du, M. H.; Long, L. S.; Kong, X. J.; Zheng, L. S. A giant 3d-4f polyoxometalate super-tetrahedron with high proton conductivity. *Small Methods* **2020**, 2000777.
32. Li, H. L.; Lian, C.; Yin, D. P.; Yang, G. Y. Three Zr(IV)-substituted polyoxotungstate aggregates: Structural transformation from tungstoantimonate to tungstophosphate induced by pH. *Inorg. Chem.* **2020**, *59,* 12842−12849.
33. Sun, Y. C.; Xie, S. S.; Tang, Z. G.; Zhao, J. W.; Chen, L. J. An innovative Sb^{III}-W^{VI}-cotemplated antimonotungstate with potential in sensing paroxetine electrochemically. *Inorg. Chem.* **2024**, *63,* 7123−7136.
34. Xiong, M. H.; Wang, X. Y.; Ji, S. D.; Liu, Y. N.; Zhao, H. N.; Gong, Z. X.; Wang, H. Y.; Niu, J. Y.; Zhang, D. D. A tetranuclear thorium-containing hexameric antimonotungstate: Synthesis, structure, and catalysis of the Knoevenagel condensation. *Inorg. Chem.* **2026**, *65,* 6802−6810.
35. Kortz, U.; Savelieff, M. G.; Bassil, B. S.; Dickman, M. H. A Large, Novel Polyoxotungstate: $[As^{III}_6W_{65}O_{217}(H_2O)_7]^{26-}$. *Angew. Chem. Int. Ed.* **2001**, *40*, 3384−3386.
36. Zhang, M.; Liu, L. H.; Song, Y. Z.; Hou, M. M.; Ma, P. T.; Han, Q. X. Designing Sb bridged polyoxotungstates for efficiently catalytic oxidation of benzyl alcohol. *J. Catal.* **2025**, *443,* 115957.
37. Dai, Y. C.; Zhang, S. Y.; Xiao, X. X.; Li, M. J.; Liu, J. C.; Chen, L. J.; Zhao, J. W. A double-tartrate-bridged deca-nuclearity europium-tungsten cluster embedded selenotungstate and its selective optical sensing of o-nitrophenol. *Polyoxometalates* **2023**, *2,* 9140041.
38. Zhao, Y.; Liu, Z. R.; Qin, Z. J.; Wen, Q. L.; Du, J.; Ren, X. Y.; Chen, C. Q.; Peng, X. C.; Kortz, U.; Yang P. Biomimetic hierarchical construction of anti-tumor polyoxopalladates for cancer therapy. *Angew. Chem. Int. Ed.* **2025**, *64,* e202505564.
39. Tong, K. W.; Wang, Y. H.; Du, J.; Chen, C. Q.; Lan, Y. Q.; Yang, P. Splicing them together: Construction of polyoxovanadate-organic polyhedra-based pyrgoscages and catenanes. *Angew. Chem. Int. Ed.* **2025,** *64,* e202504424.
40. Niu, Y. L.; Ding, Y.; Sheng, H. X.; Sun, S.; Chen, C. Q.; Du, J.; Zang, H. Y.; Yang, P. Space-confined nucleation of semimetal-oxo clusters within a $[H_7P_8W_{48}O_{184}]^{33-}$ macrocycle: Synthesis, structure, and enhanced proton conductivity. *Inorg. Chem.* **2022,** *61,* 21024−21034.
41. Liu, L. L.; Xu, Z. Y.; Yi, P.; Chen, C. Q.; Lang, Z. L.; Yang, P. Making an inverted Keggin ion lacunary. *Chem. Sci.* **2024,** *15,* 16977.
42. Sheng, H. X.; Lin, B. Y.; Chen, C. Q.; Du, J.; Yang, P. From confined growth to enhanced

peroxidase-like activity: Nucleation of a phosphate-mediated Fe^{III}–Ce^{III}–oxo cluster inside the {P_8W_{48}} nanoreactor. *Polyoxometalates* **2024**, *3,* 9140060.
43. Liu, S. R.; Chen, H. T.; Zhang, X. T. Bifunctional {$Pb_{10}K_2$}-organic framework for high catalytic activity in cycloaddition of CO_2 with epoxides and Knoevenagel condensation. *ACS Catal.* **2022,** *12,* 10373−10383.
44. Li, H. L.; Yang, G. Y. New {Co_9} cluster-added banana-shaped polyoxometalate modified by B atom. *Polyoxometalates* **2023**, *2,* 9140034.
45. Zuo, Y. K.; Li, Y. R.; Sun, Y. Q.; Li, X. X.; Sun, C.; Zheng, S. T. Efficient catalysis of Knoevenagel condensation by 1D copper-containing heteropolyoxoniobate at room temperature. *Inorg. Chem. Front.* **2024**, *11,* 1993−1997.
46. Sun, Y. H.; Cai, M. Z.; Chen, H. H.; Ma, P. T.; Niu, J. Y.; Wang, J. P. High-nuclearity Ag-substituted tetrameric sandwich-type polyoxometalates for excellent catalytic performance in C–C bond formation. *Inorg. Chem. Front.* **2025**, *12,* 7573−7580.

Table of Contents

A family of Sb^{III}-containing polyoxotungstates has been constructed with tunable aggregation state and Sb content. The ready accessibility of the strongly Lewis acidic Sb^{III} sites endows the functionalized POMs with remarkably improved catalytic activity in the Knoevenagel condensation.